Tectonics®

RESEARCH ARTICLE
10.1029/2021TC007158

Key Points:

- Geodynamic numerical models of lithosphere extension and post-rift salt tectonics quantify different types of salt flow on rifted margins
- The models show that updip extension balances largely with downdip diapir shortening, but salt nappe advance is mostly unrelated to these
- Salt nappes form by late syn-rift salt stretching and post-rift pressure-driven salt flow and are largely disconnected from updip extension

Supporting Information:

Supporting Information may be found in the online version of this article.

Correspondence to:

L. M. Pichel,
Leonardo.M.Pichel@uib.no

Citation:

Pichel, L. M., Huismans, R. S., Gawthorpe, R., Faleide, J. I., & Theunissen, T. (2022). Late-syn- to post-rift salt tectonics on wide rifted margins—Insights from geodynamic modeling. *Tectonics*, *41*, e2021TC007158. https://doi.org/10.1029/2021TC007158

Received 6 DEC 2021
Accepted 8 JUL 2022

Author Contributions:

Conceptualization: Leonardo M. Pichel, Ritske S. Huismans
Data curation: Leonardo M. Pichel
Formal analysis: Leonardo M. Pichel, Ritske S. Huismans
Funding acquisition: Ritske S. Huismans
Investigation: Leonardo M. Pichel
Methodology: Leonardo M. Pichel, Ritske S. Huismans, Thomas Theunissen
Project Administration: Ritske S. Huismans
Software: Leonardo M. Pichel, Ritske S. Huismans, Thomas Theunissen

Late-Syn- to Post-Rift Salt Tectonics on Wide Rifted Margins—Insights From Geodynamic Modeling

Leonardo M. Pichel[1], Ritske S. Huismans[1], Robert Gawthorpe[1], Jan Inge Faleide[2], and Thomas Theunissen[1]

[1]Department of Earth Science, University of Bergen, Bergen, Norway, [2]Department of Geosciences, University of Oslo, Oslo, Norway

Abstract Rifted margins are often associated with widespread and thick evaporite (salt) deposits and pronounced salt tectonics. The largest salt basins formed during the latest stages of rifting, immediately prior to continental breakup. Salt tectonics along these rifted margins commonly exhibit structural domains characterized by gravity-driven updip extension, translation, downdip shortening, and salt nappe advance. The precise spatial and temporal links between these structural processes, their relative contributions and dynamics are still a topic of debate on many margins. We use 2D thermo-mechanically coupled finite-element modeling of lithospheric extension to investigate the evolution of salt tectonics along wide rifted margins and the interplay between rifting and post-rift deformation. The models integrate lithospheric extension with post-rift salt tectonics using a geodynamically self-consistent approach where the geometries of the lithosphere and salt basins are not prescribed. They confirm that wide salt-bearing rifted margins are characterized by gravity-driven updip extension and downdip shortening, but also that syn-depositional salt flow and salt stretching occurs in their distal portions prior to and during continental breakup. This produces widening of the basin and emplacement of a salt nappe over newly formed oceanic crust. Post-rift updip extension is mostly balanced by downdip diapir shortening, all related to Couette flow. The salt nappe initiated by late syn-rift stretching advances further by post-rift pressure-driven Poiseuille salt flow so that its final width is a product of both processes. The results can be directly compared to examples from various salt-bearing rifted margins and improve our understanding of their enigmatic genesis and evolution.

Plain Language Summary Rifting of the continental lithosphere may lead to continental breakup and formation of passive margins. These margins often exhibit thick rock-salt deposits which are deposited in hypersaline basins, and which deform in a ductile, flow-like manner, developing highly complex tectonic structures. Salt deformation in these settings is commonly characterized by linked domains of updip extension, translation, downdip shortening and distal salt advance. However, the precise spatial and temporal links between these processes and their contribution to the overall salt flow are still a topic of debate. In this paper, we use 2D thermo-mechanical numerical models to explore how these salt basins develop and their interplay with continental rifting. The models show that typical, wide margin salt basins are characterized by broadly balanced post-rift updip extension and downdip shortening, but that the salt starts to deform during its deposition due to ongoing continental rifting in the distal margin. This stretches the distal salt and emplaces an allochthonous salt sheet over newly-formed oceanic crust, which is later amplified sediment-load-driven salt flow. These results can be directly compared to examples from various salt-bearing margins and improve our understanding of their enigmatic genesis and evolution.

1. Introduction

Rifted margin salt basins occur along large portions of the South and Central Atlantic, the Gulf of Mexico and the Red Sea (Figures 1a–1c). There, salt is deposited rapidly (<3 Myr) during the latest stages of rifting, after most of the crustal extension ceased, but prior to continental breakup (Davison et al., 2012; Huismans & Beaumont, 2014; Kukla et al., 2018; Rowan, 2014; 2020). Salt thus forms a contiguous, 2–4 km thick deposit across the conjugate margins, later separated by continental breakup and oceanic spreading (Davison et al., 2012; Hudec et al., 2013; Kukla et al., 2018; Lentini et al., 2010; Norton et al., 2016). The initial salt basin geometry and base-salt topography across most of these margins is therefore related to relief inherited from inactive rift structures and, in their most distal portions, to ongoing rifting and continental breakup (Figure 1) (Hudec et al., 2013; Kukla et al., 2018; Rowan, 2014). Rifted margin salt basins may also form during the earlier stages of rifting, as is the case along the

Supervision: Ritske S. Huismans, Robert Gawthorpe, Jan Inge Faleide
Validation: Ritske S. Huismans, Robert Gawthorpe, Jan Inge Faleide
Visualization: Leonardo M. Pichel, Thomas Theunissen
Writing – original draft: Leonardo M. Pichel
Writing – review & editing: Ritske S. Huismans, Robert Gawthorpe, Jan Inge Faleide

Iberia and Newfoundland margins and in fossil margins that are now inverted and incorporated into the Alps and Pyrenees (Burrel & Teixell, 2021; Ford & Vergés, 2021; Roca et al., 2021; Rowan, 2014; Walker et al., 2021).

Salt tectonics along rifted margins with late to early post-rift salt is commonly described as a product of post-rift gravity-driven deformation caused by the seaward tilt of the margin in response to thermal subsidence, and by differential sediment loading forming kinematically-linked domains of updip extension, translation and downdip shortening (Figure 1d) (Brun & Fort, 2011; Hossack, 1995; Jackson, Jackson, & Hudec, 2015; Jackson, Jackson, Hudec, & Rodriguez, 2015; Marton et al., 2000; Peel, 2014; Rowan et al., 2004). The updip extensional domain is characterized by seaward salt evacuation and development of listric normal faults cored by triangular reactive diapirs in their footwall and associated with rollovers. Typically, these faults accommodate together a total of 10–30 km of extension, although some ultra-wide margins are also shown to have up to ∼50 km of extension (cf., Rowan et al., 2021) (Figures 1a–1c). The extensional domain transitions seaward into a 40–80 km wide domain of salt and overburden translation in the order of 20–30 km and multiphase salt deformation driven by salt flow variations over base-salt relief (Figures 1a–1c) (Dooley et al., 2017; Erdi & Jackson, 2021; Peel, 2014; Pichel et al., 2019, 2020). The translation domain passes downdip into the shortening domain defined by a 40–100 km wide area of salt inflation and buckle-folding with intense diapirism and 10–50 km wide allochthonous salt nappes emplaced over younger, recently generated oceanic crust and/or post-salt sediments (Figures 1a–1c) (Hudec & Jackson, 2004; Hudec & Norton, 2019).

Updip extension in salt-bearing rifted margins is interpreted to balance with downdip shortening (Hossack, 1995; Jackson, Jackson, & Hudec, 2015; Peel, 2014; Rowan & Ratliff, 2012). However, solving the balance of deformation is often problematic owing to overprinting of extensional and contractional domains, the effects of base-salt relief, and the mobile nature of salt which can accommodate shortening and/or extension cryptically by diapir squeezing or widening (Brun & Fort, 2011; Dooley et al., 2018; Hossack, 1995; Hudec & Jackson, 2004; Jackson, Jackson, & Hudec, 2015; Pichel et al., 2018, 2019, 2020; Rowan & Ratliff, 2012). Salt tectonics in these systems can be understood by considering the relative contributions of Couette and Poiseuille salt flows (cf. Gemmer et al., 2004; Jackson & Hudec, 2017). In Couette flow, the salt is deformed by layer-parallel simple shear as the overburden translates laterally. In Poiseuille flow there is pressure-driven lateral expulsion of the salt underneath an overburden of variable thickness which does not fail or translate laterally, that is, only the salt translates (Gemmer et al., 2004; Jackson & Hudec, 2017; Rowan et al., 2004; Turcotte & Schubert, 2002). Solving the balance of salt-related deformation and the contribution between different types of flow and structural processes (i.e., extension, shortening, translation) allows quantification and restoration of salt-related deformation along rifted margins (Jackson, Jackson, & Hudec, 2015; Jackson, Jackson, Hudec, & Rodriguez, 2015; Rowan & Ratliff, 2012).

Another important aspect of these margins is that the architecture and nature of the distal margin and the precise location of the continent-ocean boundary (COB) are often not well constrained. For example, the interpretations for this domain range from exhumed mantle or lower crust to extended/intruded continental crust, volcanics and/or oceanic crust owing to limitations in seismic imaging underneath thick and highly deformed salt layers (Blaich et al., 2011; Epin et al., 2021; Evain et al., 2015; Fernandez et al., 2020; Kumar et al., 2013; Norton et al., 2016; Unternehr et al., 2010; Zalán et al., 2011). Understanding the relationship between the style and dynamics of distal salt tectonics with the underlying basement has thus important implications for understanding distal margin architecture and for producing accurate plate kinematic reconstructions.

However, while regional salt tectonics has been extensively investigated along rifted margins, very few studies have analyzed the link between crustal-scale rift architecture, salt deposition, and salt tectonics (Epin et al., 2021; Fernandez et al., 2020; Hudec & Jackson, 2004; Jackson, Jackson, & Hudec, 2015; Jackson, Jackson, Hudec, & Rodriguez, 2015; Kukla et al., 2018; Peel et al., 1995; Pichel & Jackson, 2020; Pichel et al., 2021; Rowan, 2020; Tari et al., 2017). Even fewer (Allen & Beaumont, 2016; Allen et al., 2020; Curry et al., 2018) have attempted to model this and none have addressed the role rifting and syn-rift salt deposition play on post-rift gravity-driven salt tectonics. We thus use a 2D geodynamic numerical modeling technique that combines lithospheric extension and break-up, syn- and post-rift sedimentation to simulate the birth and evolution of rifted margin salt basins. The models do not prescribe the geometries of the lithosphere and of the salt basins allowing a self-consistent evolution of both syn- and post-rift deformation. The dynamic models afford quantification of the respective contributions of updip extension, translation, diapir shortening, salt nappe advance, and the different types of salt flow to rifted margin salt tectonics. Our results present unprecedent detail for syn- and post-rift stratigraphy and salt structures that can be directly compared to natural examples from various rifted margins and explain the processes controlling margin-scale salt tectonics.

10.1029/2021TC007158

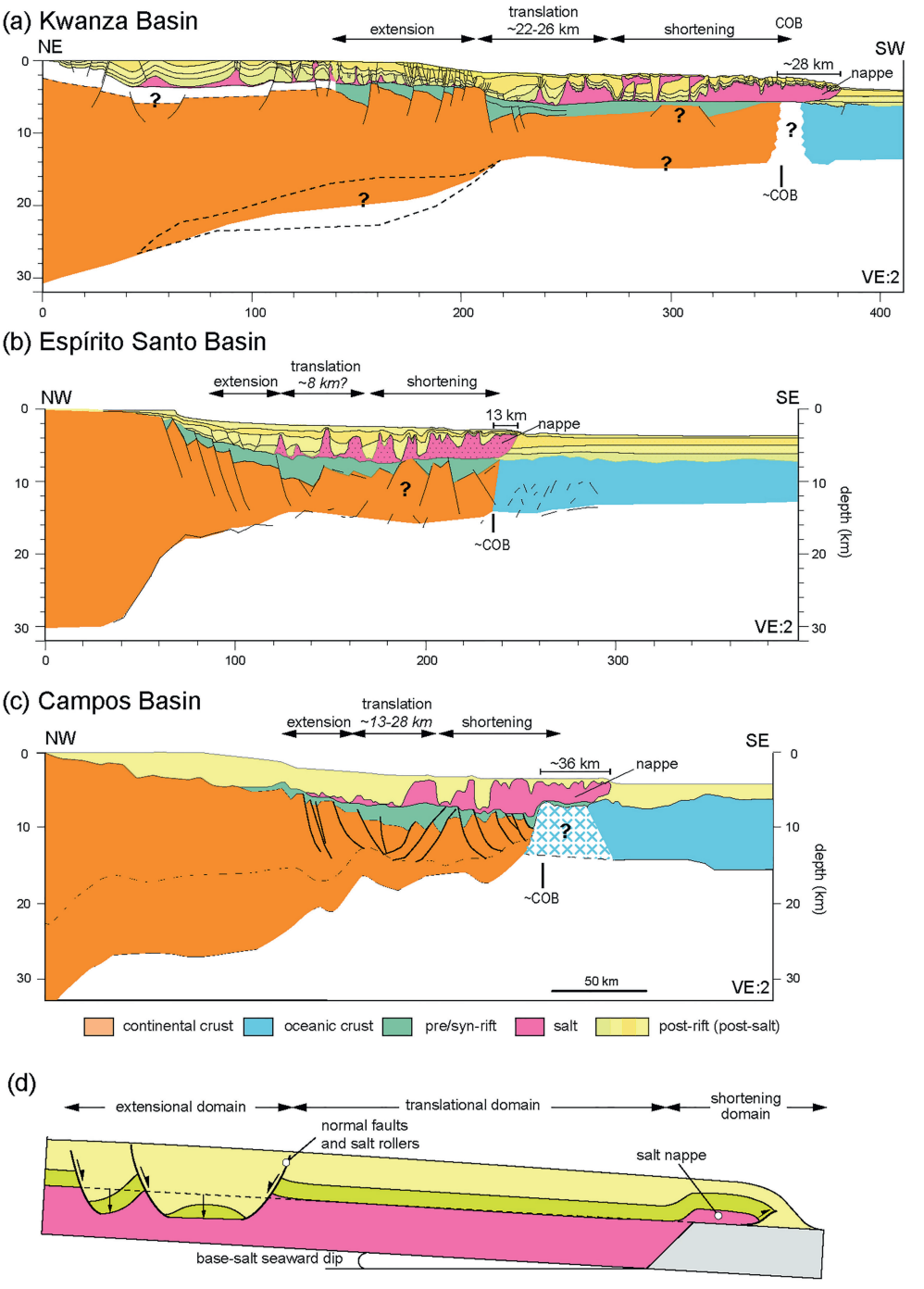

Figure 1. Regional profiles showing crustal-scale architecture and salt tectonics across (a) Kwanza Basin, Angola, (b) Espirito Santo, Brazil (adapted from Blaich et al., 2011), and (c) Campos Basin, Brazil (adapted from Zalán et al., 2011). (d) Schematic cross-section (adapted from Jackson, Jackson, & Hudec, 2015; Jackson, Jackson, Hudec, & Rodriguez, 2015) illustrating the current knowledge of salt tectonic deformation along rifted margins characterized by linked and balanced domains of updip extension, translation, and downdip shortening associated with salt nappe advance.

2. Data and Methods

2.1. Numerical Methods

We use an arbitrary Lagrangian-Eulerian (ALE) thermo-mechanically coupled finite element method for the solution of plane strain, incompressible viscous-plastic creeping flows (Erdős et al., 2014; Theunissen & Huismans, 2019; Thieulot, 2011). The method solves the force balance equations of equilibrium for quasi-static incompressible flows (Stokes) in two dimensions coupled with the time-dependent heat conservation equation. The mechanical and thermal evolution are coupled through nonlinear temperature- and pressure-dependent rheologies in addition to the temperature dependence of buoyancy (Huismans & Beaumont, 2011; Theunissen & Huismans, 2019).

When the stress state is below the frictional-plastic yield stress, the flow is viscous and is defined by temperature-dependent nonlinear power law rheologies based on laboratory measurements on "wet" quartz (Gleason & Tullis, 1995) and "wet" olivine (Karato & Wu, 1993). The effective viscosity, μ_{eff}, in the power law rheology is:

$$\mu_{\text{eff}} = f A^{-1/n} \dot{E}_2^{(1-n)/2n} e^{\frac{Q+Vp}{nRT}}$$

where $\dot{E}_2$ is the second invariant of the deviatoric strain rate tensor $1/2\,(\dot{\varepsilon}_{ij}\dot{\varepsilon}_{ij})$, A is the preexponential scaling factor, n is the power law exponent, Q is the activation energy, R is the universal gas constant, and V is the activation volume. The factor f is used to scale viscosities calculated from the reference quartz and olivine flow laws, thereby producing strong and weak versions of these materials. Frictional-plastic yielding is modeled with a pressure-dependent Drucker-Prager yield criterion which is equivalent to the Coulomb yield criterion for incompressible deformation in plane strain. Yielding occurs when:

$$\sigma_y = \sqrt{J_2} = C\cos(\phi_{\text{eff}}) + P\sin(\phi_{\text{eff}})$$

where J_2 is the second invariant of the deviatoric stress tensor, C is the cohesion, ϕ_{eff} is the effective internal angle of friction following $P \cdot \sin(\phi_{\text{eff}}) = (P - P_f)\sin(\phi)$ and P_f is the pore fluid pressure. This yield criterion approximates frictional sliding (i.e., faulting) in rocks, and includes pore-fluid pressure effects.

Plastic flow is incompressible. Frictional-plastic strain softening is introduced by a linear decrease of $\phi_{\text{eff}}(\varepsilon)$ from 15° to 2° and $C(\varepsilon)$ from 20 to 4 MPa with respect to plastic strain (ε) (Buck, 1993; Huismans & Beaumont, 2002; Lavier et al., 1999, 2000). The plastic strain is updated at every time-step with the second invariant of the deviatoric strain. To avoid artificial grid dependent strain weakening the grid is purposely uniform in the domain where most strain localization occurs (see Theunissen & Huismans, 2019; Thieulot, 2011). A complete description of the numerical modeling approach and the governing equations is provided in the Supporting Information S1. A complete list of material parameters is given in Table 1.

2.2. Model Setup

The models are designed using a rheologically layered lithosphere comprising a 35 km-thick crust and 90 km mantle lithosphere above a sublithospheric mantle in a 600 km-high and 1,200 km-wide model domain (Figure 2a). The uppermost 3 km of the crust corresponds to pre-rift sediments with the same rheology as the upper crust. The Eulerian grid consists of 2,400 in the horizontal and 290 elements in the vertical direction. The distribution of the elements in the vertical direction is irregular, allowing for high resolution in the upper crust of $\Delta z = 200$ m in the shallowest 20 km, $\Delta z = 625$ m between 20 and 70 km, $\Delta z = 1{,}100$ m between 70 and 120 km, and $\Delta z = 7{,}917$ m between 120 and 600 km of depth. The resolution in the horizontal direction is 500 m for the entire model domain. Extensional horizontal velocity conditions ($v = \pm 0.5$ cm/year) are applied to the lithosphere, and the corresponding exit flux is balanced by a low velocity inflow in the sublithospheric mantle (Theunissen & Huismans, 2019). The top of the model is a free surface, and the sides and base are free slip boundaries (Figure 2a).

For the thermal boundary conditions, we specify a basal temperature of 1,520°C and insulated lateral boundaries. The initial temperature field is laterally uniform and increases with depth from the surface ($T_{\text{surf}} = 0$°C) to the base of the crust (Moho temperature, $T_{\text{moho}} = 550$°C) with a surface heat flux of 55.3 mW/m^2. Below the Moho, temperature linearly decreases to the base of mantle lithosphere (initially at $T_{\text{LAB}} = 1{,}328$°C). The temperature

Table 1
Parameters for the Lithosphere-Scale Thermo-Mechanical Models of Salt-Bearing Wide Rifted Margins

Parameter	Symbol	Units	Salt	Sediments	Upper crust (0–25 km)	Lower crust (25–35 km)	Lithospheric mantle	Sub-lithospheric mantle
Rheological parameters								
Effective viscosity range	μ_{eff}	Pa.s	10^{18}, 5×10^{18}, 10^{19}	10^{18}–10^{27}	10^{18}–10^{27}	10^{18}–10^{27}	10^{18}–10^{27}	10^{18}–10^{27}
Angle of internal friction	ϕ_{eff}	–	–	15	15		15	
→ after strain weakening	ϕ_{eff}	–	–	2	2		4	
Initial cohesion	C	MPa	–	10	20		20	
→ after strain weakening	C	MPa	–	4	4		20	
Strain weakening range	–	–	–			0.05–1.05		
Flow law	–	–	–		WQtz[a]		WO[b]	
Scaling factor	fc	–	–	1	0.1		5	1
Power law exponent	n	–	–	4	4		3	
Activation energy	Q	kJ/mol	–	222.81	222.81		429.83	
Constant	A	Pa^{-n}/s	–		8.574×10^{-28}		1.758×10^{-14}	
Activation volume	V	m^3/mol	–		0.0		15×10^{-6}	
Density at $T_0 = 273$ K	ρ_0	kg/m^3	2,200	2,400	2,750	2,900	3,300	
Thermal parameters								
Thermal conductivity	k	W/m/K		2.25			2.25–5.6	
							2.25–51.46	
Heat capacity	c_p	J/K/kg	803.57		818.18	775.86	681.81	
Thermal diffusivity	κ	m^2/s		1.0×10^{-6}			$1–2.5 \times 10^{-6}$	
							$1–22.87 \times 10^{-6}$	
Heat production rate	H	W/m	0.8×10^{-6}		1.12×10^{-6}	0.48×10^{-6}	0	
Thermal expansion	α_T	1/K	3×10^{-5}			3.1×10^{-5}		
Boundary conditions								
Surface temperature	T_{surf}	°C			0			
Pre-rift sediment thickness	$h_{pre\text{-}sed}$	km			3			
Initial Moho depth	d_{moho}	km			35			
Moho Temperature	T_{moho}	°C			550			
LAB depth	d_{LAB}	km			125			
LAB temperature	T_{LAB}	°C			1,328			
Basal temperature	T_{LM}	°C			1,520			
Extension velocity	V_{ext}	cm/year			1			

Note. Flow laws are based on power law with creep parameters from wet quartz (Gleason & Tullis, 1995) and wet olivine (Karato & Wu, 1993). Values are given with two digits precision. WQtz = wet quartz; WO = wet olivine; LAB = Lithosphere-Asthenosphere Boundary.
[a]Dislocation creep models for WQtz. [b]Dislocation creep models for WO.

of the sublithospheric mantle follows an adiabatic gradient (0.4°C/km). Thermal conductivity linearly increases to 51.46 W/m/K at 1,350°C (~125 km depth), consistent with scaling the thermal conductivity of upper mantle convection by the Nusselt number (Theunissen & Huismans, 2019). The enhanced conductivity maintains a nearly constant heat flux to the base of the lithosphere and an adiabatic temperature gradient in the sublithospheric mantle (e.g., Pysklywec & Beaumont, 2004).

The initial strain field is defined by a white noise that corresponds to an inherited domain of mechanical heterogeneity and weakness by a tapered symmetrical 400 km wide area in the center of the model so that the orientation of faults and rift geometries are not prescribed and are generated spontaneously (Figure 2a). The plastic strain (ε) is initialized with white noise that has a Gaussian distribution with a mean value of 0.3 and a maximum of 0.8.

10.1029/2021TC007158

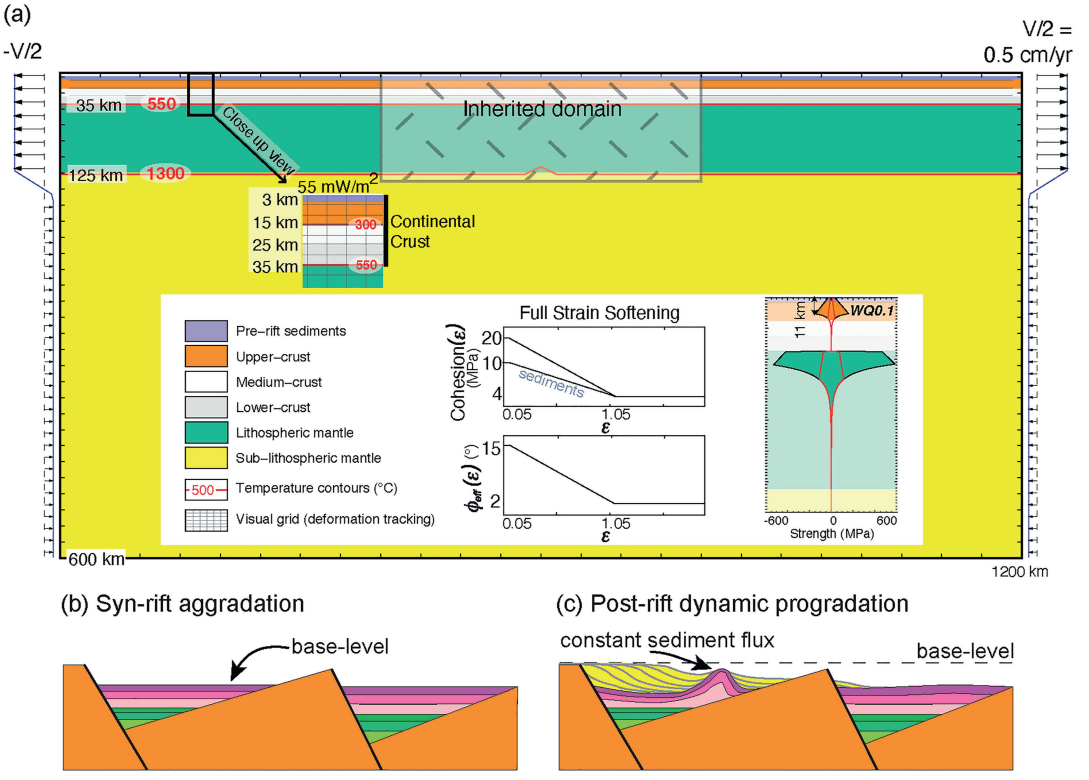

Figure 2. (a) Model setup showing rheological-layered structure, boundary conditions, initial thermal state, and frictional-plastic strain softening conditions. The values used for the mechanical and thermal parameters are listed in Table 1. (b) Schematic diagram illustrating syn-rift aggradation for pre- and salt sediments in which sediments aggrade toward local basement minima. (c) Schematic diagram illustrating post-rift (post-salt) dynamic progradation in which the depositional profile changes in shape and length through time according to the evolving salt topography.

A small thermal heterogeneity is introduced at the base of the lithosphere in the model center in order to enhance rift localization.

The crust follows a wet quartz rheology (Gleason & Tullis, 1995) with a scaling factor (f_c) of 0.1, based on previous experiments from Theunissen and Huismans (2019). This corresponds to a weak crustal rheology that results in development of wide rifted margins which are characteristic of salt basins in most of the South Atlantic and Gulf of Mexico (see Theunissen & Huismans, 2019 for details on scaling). The densities of crust, mantle lithosphere, and sub-lithospheric mantle are calibrated so that the depth of the modeled mid-ocean ridge spreading system fits with global observations of average mid-ocean ridge depth. We do not include any melt generation and/or magmatism for model simplification purposes (cf., Theunissen & Huismans, 2019), as this is beyond the scope of this study, and beyond the state-of-art of geodynamic models of lithospheric extension (cf., Lu & Huismans, 2022). The oceanic crust is thus simulated by a phase-change of the sub-lithospheric mantle when it reaches the upper 6 km of the lithosphere. This involves changes in density (from 3,300 to 2,900 kg/m^3) and material color (light yellow to green), all other properties are kept constant (Figures 2a and Table 1).

Salt is treated as a linear viscous material and all models have a constant salt viscosity. The reference model has an intermediate salt viscosity of 5×10^{18} Pa s, and we also perform sensitivity tests with low (10^{18} Pa s) and high (10^{19} Pa s) salt viscosities. These values are based on laboratory experiments of halite deformation (van Keken et al., 1993: Urai et al., 2008) and numerical models simulating salt flow (cf., Gemmer et al., 2004; Albertz & Ings, 2012; Allen & Beaumont, 2016).

2.3. Sedimentation

Sedimentation occurs by filling all accommodation between the model surface and a defined base(sea)-level with sediments at each time step. We implement two different styles of sedimentation in our models, aggradation for

syn-rift clastics and salt (Figure 2b), and post-rift progradation using a dynamic depositional profile (Figure 2c) (Theunissen & Huismans, 2019). We also apply a new novel tracking method based on Lagrangian surface descriptions that allows to resolve the internal stratigraphic architecture of the salt and post-salt intervals with greater detail than previous studies (Allen & Beaumont, 2016; Goteti et al., 2013).

All models include water-load and syn-rift (pre-salt) aggradation at 25 m/Myr below a −1 km base-level (i.e., sea-level measured with respect to a reference column of continental lithosphere). This is followed by salt aggradation at 2 km/Myr below −750 m of sea-level during the last 1 Myr of rifting. Aggradation is defined with a horizontal bathymetric profile with a vertical position that is adjusted for each main depositional stage, that is, syn-rift clastic and salt deposition (Figure 2b). In this approach, the syn-rift sediments (clastics and salt) aggrade in local basement minima. The rate of sedimentation is kept constant through time but the shape of the sediment package changes in response to changes in basin geometry so that the volume of sediment is kept constant in this approach (see Theunissen & Huismans, 2019). Salt is deposited rapidly during the last ∼2 Myr of the syn-rift, when extension is localized in the outermost margin, prior to breakup and development of oceanic crust. The salt thus forms a contiguous basin across both conjugate margins (Figure 2b). The relative timing and rate of salt deposition and the sedimentation rates are consistent with most studies of salt-bearing rifted margins (Davison et al., 2012; Hudec et al., 2013; Kukla et al., 2018; Lentini et al., 2010; Rowan, 2014).

Post-rift dynamic progradation occurs at −250 m of base-level with a constant sediment flux of 0.001 m^3/s (∼31,6 km^3/Myr) for all models and is consistent with post-rift sediment fluxes ranging from 0.3 to 52 km^3/Myr along the South Atlantic African margins (cf. Baby et al., 2020). Post-rift dynamic progradation deposition, $d_{offshore}$, is controlled by specifying a constant sediment flux, Q_s, to the basin with deposition based on a characteristic sediment transport length L_d (30 km in our models) following:

$$d_{\text{offshore}} = Q_s \frac{dx}{L_d}$$

where Q_s is the sediment discharge per unit width (e.g., Theunissen & Huismans, 2019).

Syn- and post-rift sediments have an average density of 2,400 kg/m^3 whereas the salt has a density of 2,200 kg/m^3. We do not incorporate compaction (neither lateral nor vertical) in our models for simplification purposes.

3. Results

3.1. Reference Model 1—Intermediate Salt Viscosity

Rifting of weak crust results in the development of two ca 250 km wide conjugate margins with 140–160 km wide salt basins on each of these (Figure 3a). Salt deposition occurs between 17 and 18 Myr, during the final stage of rifting, and is followed by breakup and initiation of oceanic crustal spreading at c. 21 Myr (Figures 3a and 3b, Movie S1). Both margins are defined by proximal symmetric grabens that pass seaward into half-grabens bounded by large-offset, low-angle normal faults that exhume middle and lower crust in the distal domain (Figure 3a). These pass seaward into 30–60 km wide areas of highly thinned, <7 km thick crust, and a 20 km wide outer high in the distal margin (Figure 3). The grabens are filled with pre-salt syn-rift sediments that are 0.5–1 km thick, whereas the highs receive much less (<0.4 km) syn-rift sediments. The salt thickens seaward, reaching up to 3–4 km in thickness in the deepest basin adjacent to the outer high (Figure 3a). The depositional salt thickness varies with base-salt topography in the proximal domain, producing semi- to fully disconnected salt basins. In the distal domain, there is development of syn-salt deposition intra-salt minibasins associated with crustal extension (Figure 3a).

Shortly after breakup, at 24 Myr, the left-margin proximal domain is characterized by minor diapirism (<2 km of height) and folding above the semi-isolated, proximal salt sub-basins where prograding sediments are deposited (Figure 3b). At this stage, there is very minor salt expulsion and folding at the transition to the distal domain and negligible seaward salt translation over the distal margin, as seen by the broadly flat and undeformed intra- and top-salt layers (Figure 3b). The distal edge of the salt basin is characterized by thinning and stretching, with development of ∼15 km wide salt nappes on top of the early oceanic crust, as the two conjugate margins separate by rifting and oceanic spreading (Figures 3b and Movie S1).

At 35 Myr, well-defined domains of updip extension and downdip shortening, connected by an intermediate zone of translation, develop on both margins (Figure 3c). The extensional domain is characterized by salt rollers

10.1029/2021TC007158

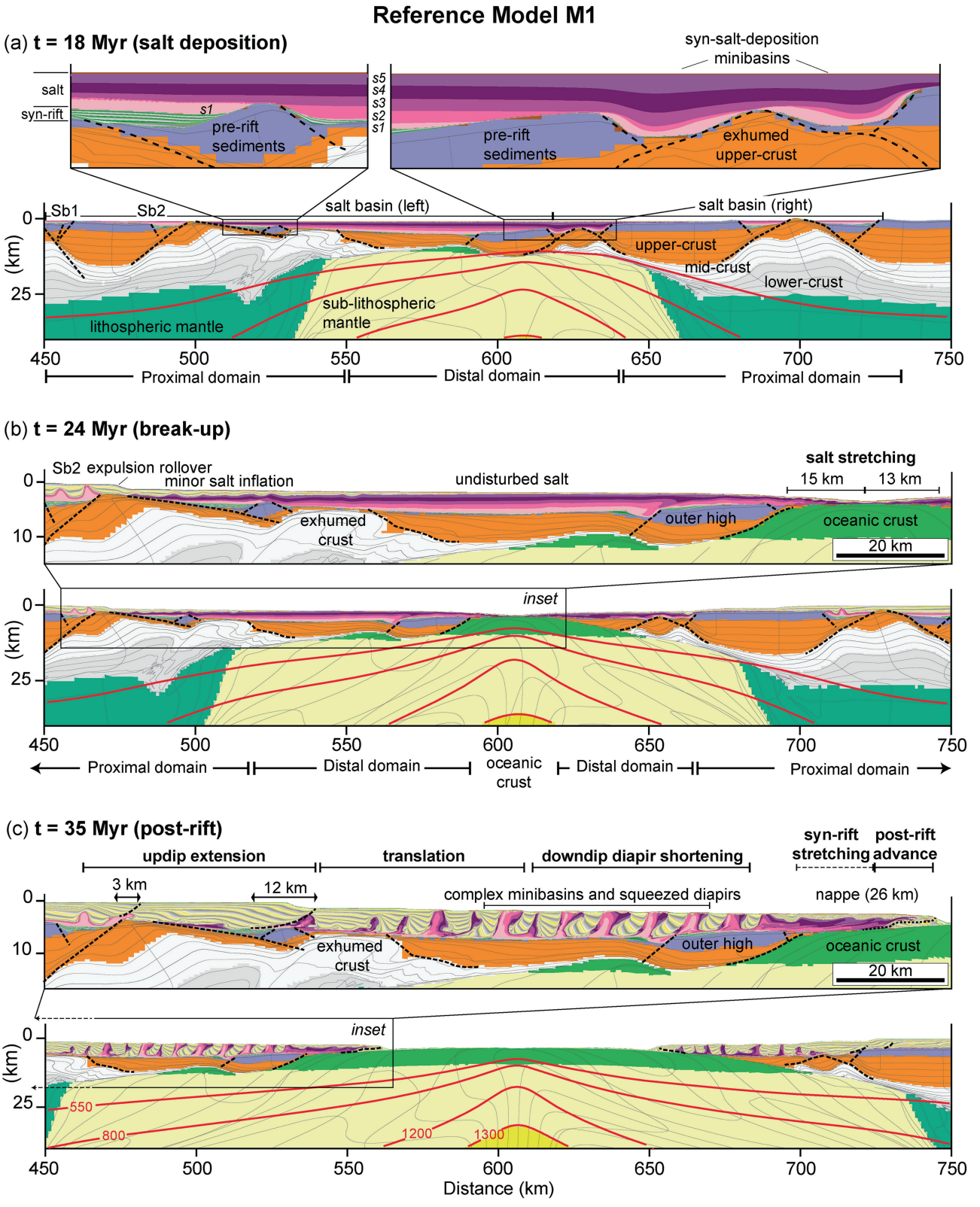

Figure 3. Reference Model 1 of a salt-bearing wide rifted margin with intermediate salt viscosity. (a) 18 Myr, time of salt-deposition immediately prior to continental breakup (20–21 Myr). (b) 24 Myr, conjugate salt basins are separated with distal salt nappe owing to stretching on top of oceanic crust. (c) 35 Myr, fully established passive margin salt tectonics with updip extension, translation, downdip diapir shortening, and salt nappe advance. Black boxes indicate zoomed domain at 24 and 35 Myr. Red lines represent geotherms. See Movie S1 for animation.

associated with landward-dipping normal faults and extensional rollovers that together accommodate ~15 km of extension (Figure 3c). The extensional domain passes downdip into an area characterized by salt and overburden translation, multiphase diapirism and complex minibasin geometries. In the distal domain a series of 3–5 km tall upright and seaward-leaning squeezed diapirs are associated with 2–3 km wide salt tongues and rotated minibasins above depleted salt (Figure 3c). The initially stretched distal end of the salt is characterized at this stage by salt thickening, folding, and seaward advance over oceanic crust and post-salt sediments, producing a 26 km wide salt nappe (Figure 3c).

3.2. Low-Viscosity Salt Model 2

At 24 Myr, low-viscosity salt model 2 exhibits greater salt mobility with formation of taller, 3–4 km high, upright diapirs and equally thick minibasins over the semi-isolated salt sub-basins in the proximal domain (Figures 4a and 4b). The transition to the distal domain shows development of an incipient seaward-dipping expulsion rollover that passes seaward onto salt anticlines and small diapirs over a minor pre-salt structural high (Figure 4b). Further seaward, subtle intra-salt folding, but negligible top- and supra-salt deformation and translation, characterize most of the distal margin (Figure 4b). As in the reference model, the distal edge of the salt basin displays thinning and stretching with development of salt nappes on top of the early oceanic crust, which are wider (~20 km), thicker (up to ~2 km) and exhibit more significant intra-salt folding compared to the reference model (Figures 4b and Movie S2). A distal supra-salt minibasin also develops in between the two nappes as they separate from each other (Figure 4b).

At 35 Myr, the domains of updip extension and downdip shortening, connected by an intermediate zone of translation, develop on both margins (Figure 4c). The style of deformation is broadly similar to the reference model, although the magnitudes of extension, shortening and translation vary significantly (see Section 3.4). The updip normal faults and associated rollovers accommodate less extension (~8 km). The complexity and frequency of squeezed diapirs in the downdip domain is greater, whereas their amplitude is less (<3.5 km) relative to the reference model (cf., Figures 3c and 4c). The distal salt nappe advances further over oceanic crust, reaching a width of ~56 km and contains salt anticlines and a few diapirs and minibasins (Figures 4c and Movie S2).

3.3. High-Viscosity Salt Model 3

At 24 Myr, high-viscosity salt model 3 shows significantly less salt deformation across the entire margin with only minor salt inflation and development of small, <1 km tall salt anticlines in the proximal domain (Figures 5a and 5b). There is also negligible salt and supra-salt deformation and translation over the distal margin, similar to the reference model (cf., Figures 3b and 5b). The distal margins exhibit intra-salt folding over the outer high and salt stretching and thinning with subtle intra- and top-salt folding producing ~3–7 km wide salt nappes over the newly formed oceanic crust (Figure 5b).

At 35 Myr, there is development of a single seaward-dipping rollover and landward-dipping normal fault that accommodates ~6 km of extension in the proximal domain, passing seaward into an area of salt and overburden translation, salt inflation, and squeezed diapirs (Figure 5c). These diapirs and their associated minibasins are generally broader, simpler, and more widely spaced in comparison to the reference model (cf., Figures 3c and 5c). The most distal diapirs are also surrounded by significant, >1 km thick salt underneath their respective minibasins as opposed to highly-depleted salt below minibasins in the reference and low-viscosity salt models (Figures 3–5). The distal salt nappe inflates and advances over the oceanic crust reaching a maximum width of ~15 km with salt and post-salt sediments developing folds, but no diapirs (Figure 5 and Movie S3).

3.4. Structural Processes and Variability With Salt Viscosity

We next quantify the various contributions to salt tectonics in the three models. The total width of the salt nappe on top of the oceanic crust (N_w) is controlled by initial syn-rift salt stretching (S) and post-rift nappe advance (A), that is,

$$N_w = S + A \tag{1}$$

Post-rift salt tectonics includes contributions from updip extension (E), diapir shortening (D_s), and pressure-driven Poiseuille flow (P). The horizontal components of salt tectonics balance (Figure 6) given:

$$A = E - D_s + P \tag{2}$$

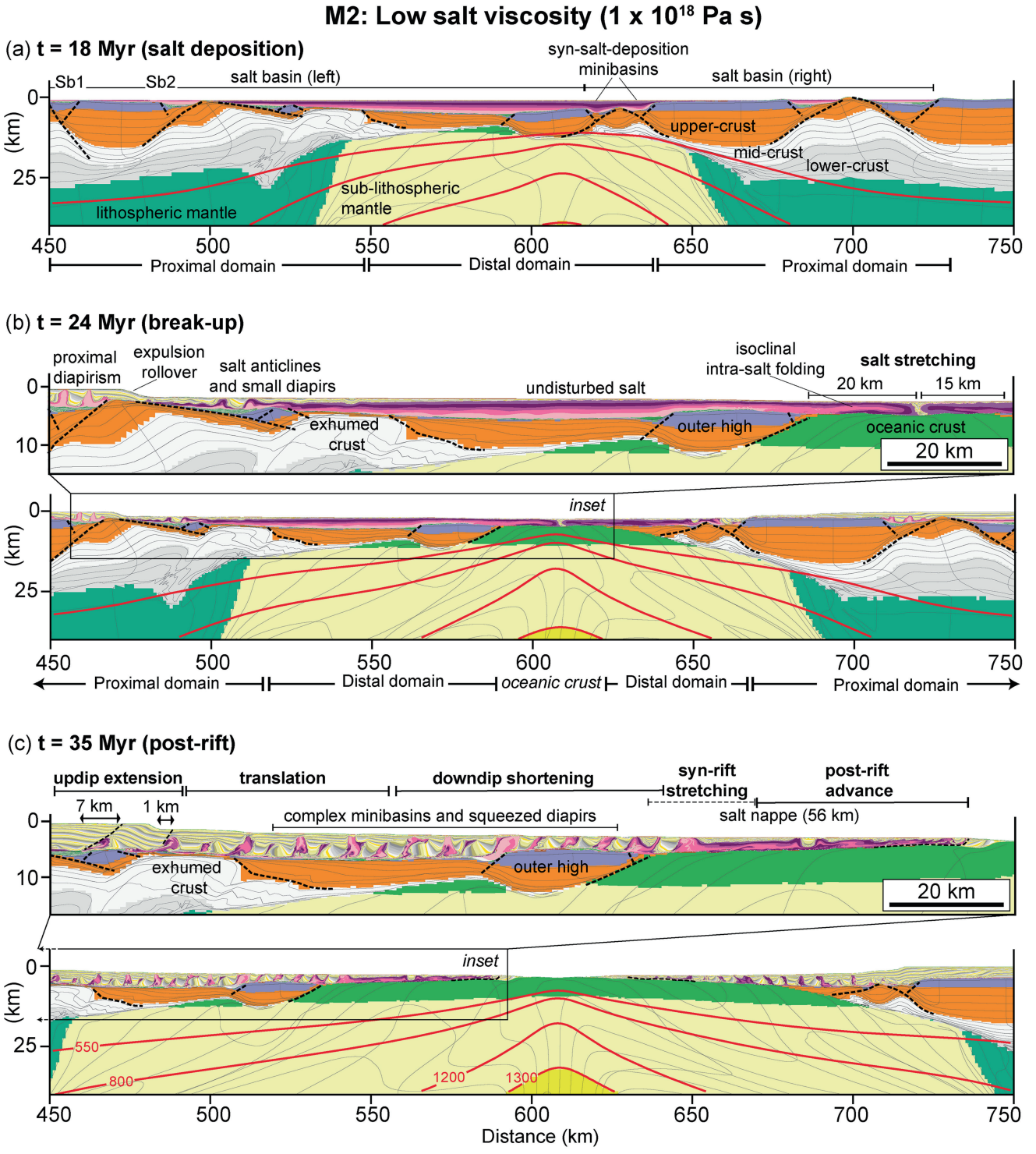

Figure 4. Low-viscosity salt Model 2, (a) 18 Myr, time of salt-deposition immediately prior to continental breakup (20–21 Myr). (b) 24 Myr conjugate salt basins are separated with development of up to 20 km wide distal salt nappes owing to stretching on top of oceanic crust. (c) 35 Myr, fully established passive margin salt tectonics with updip extension, translation, diapir shortening, and salt nappe advance. Black boxes indicate zoomed domain at 24 and 35 Myr. Red lines represent the geotherms. See Movie S2 for animation.

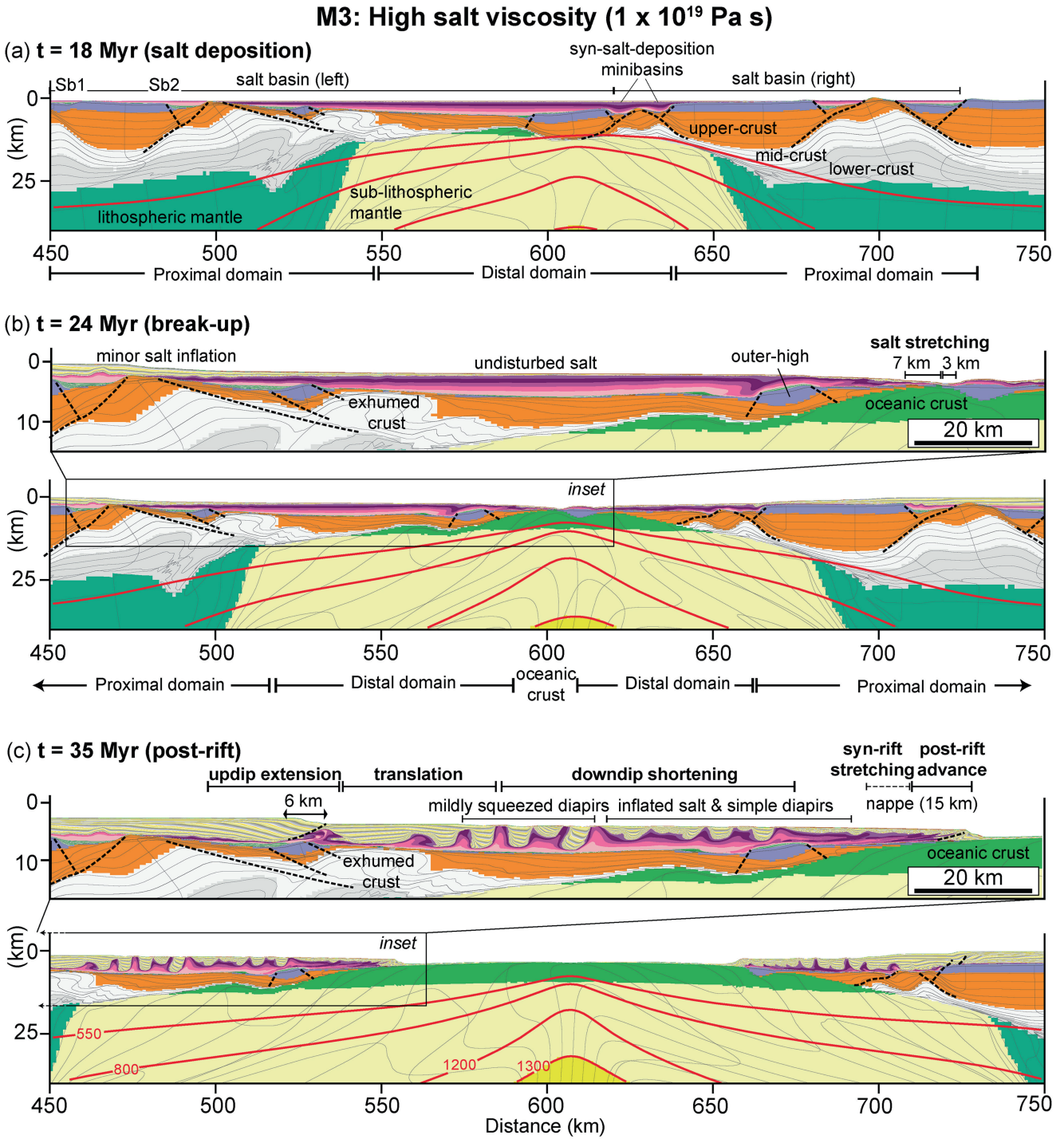

Figure 5. High-viscosity salt Model 3, (a) 18 Myr, time of salt-deposition immediately prior to continental breakup (20–21 Myr). (b) 24 Myr, conjugate salt basins are separated with development of 3–7 km wide distal salt nappes owing to stretching on top of oceanic crust. (c) 35 Myr, fully established passive margin salt tectonics with updip extension, translation, diapir shortening, and salt nappe advance. Black boxes indicate zoomed domain at 24 and 35 Myr. Red lines represent the geotherms. See Movie S3 for animation.

Updip extension (E) is measured by summing the heave of updip normal faults. Diapir shortening (D_s) is inferred from the amount of diapir squeezing, measured by the difference between their initial and final diapir width. The evidence of diapir shortening are: (a) the abrupt narrowing of their stems, (b) their seaward-vergence, and (c) the associated minibasin rotation. Pressure-driven Poiseuille flow (P) is not directly

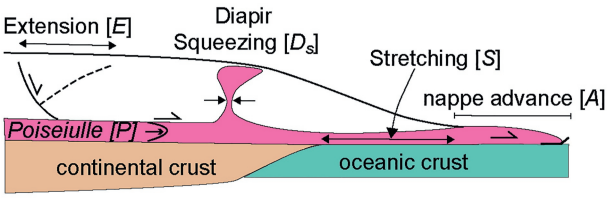

Salt nappe width: $N_w = S + A$

Salt balance: $A = N_w - S = E - D_s + P$

deformation processes (km)

μ_{salt}	N_w	S	A	E	D_s	P
1E18	56	20	36	8	8	*36*
5E18	26	15	11	15	14	*10*
1E19	15	7	8	6	5	*7*

Figure 6. Schematic diagram of balance of salt tectonics on rifted margins based on model results. Table show values of total nappe width (N_w), salt nappe stretching (S), post rift salt nappe advance (A), updip extension (E), diapir shortening (D_s), and pressure driven flow (P) for models with varying salt viscosity.

measured because it varies along the model profile, however its contribution to lateral salt nappe advance is inferred by balancing salt deformation using Equation 1 above. The magnitude of the respective contributions to salt tectonics varies between the models. For reference model 1, allochthonous salt on oceanic crust by salt stretching S = 15 km. At 35 Myr, model 1 exhibits a total width of the salt nappe N_w = 26 km, implying that post-rift nappe advance A = 11 km (Figure 6). This balances with updip salt-detached extension E = 15 km, downdip shortening by diapir squeezing D_s = 14 ± 2 km, and pressure-driven Poiseuille salt flow P = 10 km.

For low-viscosity salt model 2, allochthonous salt on oceanic crust by salt stretching S = 20 km. The total width of the salt nappe N_w = 56 km implies that post-rift nappe advance A = 36 km (Figure 6). Updip salt-detached extension E = 8 km balances with downdip shortening by diapir squeezing D_s = 8 ± 2 km, so that pressure-driven Poiseuille salt flow P = 36 km. The high-viscosity salt model 3 exhibits allochthonous salt on oceanic crust by salt stretching S = 7 km. The final salt nappe width N_w = 15 km implies that post-rift nappe advance A = 8 km (Figure 6). Updip salt-detached extension E = 6 km balances with downdip shortening by diapir squeezing D_s = 5 ± 2 km, so that pressure-driven Poiseuille salt flow P = 7 km.

In summary, total nappe width and contributions from syn-rift stretching and post-rift nappe advance increase with decreasing viscosity. Conversely, updip extension and diapir shortening increase with viscosity decreasing from 10^{19} to 5×10^{18} Pas, but then exhibit a significant decrease for salt viscosity of 10^{18} Pas. This variation in updip extension and diapir shortening with changing viscosity is mirrored by the contribution from Poiseuille flow, which exhibits a marked increase for salt viscosity 10^{18} Pas (Figure 6).

4. Discussion

4.1. Dynamics of Salt Deformation

Salt tectonics in our models exhibits three characteristic phases. (a) Syn-depositional salt flow and development of syn-salt-deposition minibasins resulting from stretching in the distal margin as salt is deposited during the last phase of rifting (Figure 7a). (b) Emplacement of distal salt nappes on the early oceanic crust by stretching above the rift axis (Figures 7b and Video S4). (c) Post-rift sediment progradation and significant salt tectonics in the form of updip extension, translation, downdip diapir shortening, and pressure-driven salt flow and nappe advance (Figure 7c).

For all models, intra-salt minibasins form during salt deposition and rifting in the distal margin. In the absence of post-salt sediment loading and intra-salt rheological variability these are interpreted as resulting from latest syn-rift salt stretching. Part of the allochthonous salt nappe on the oceanic crust results from early salt stretching which is independent of updip salt tectonics. The nappe is then amplified during the post-rift stage and advances further by lateral pressure-driven Poiseuille salt flow associated with margin-scale salt tectonics. The contribution of syn-rift stretching relative to post-rift nappe advance increases from 35% to 50% of the total nappe width with increasing salt viscosity. Quantification of the various contributions to salt tectonics in the models shows that nearly all (~90%) updip extension is balanced by downdip diapir shortening (Figure 6). This demonstrates that total salt nappe advance is controlled by the combination of syn-rift extension and post-rift pressure-driven Poiseuille flow, and that salt nappes are *not* a direct product of downdip shortening in response to updip extension as commonly envisaged (Brun & Fort, 2011; Jackson, Jackson, & Hudec, 2015; Jackson, Jackson, Hudec, & Rodriguez, 2015; Marton et al., 2000; Rowan et al., 2004).

The models provide further insight into the complex link between updip extension, translation, downdip diapir shortening and nappe advance, and their respective dynamics of salt flow. Post-rift sediment progradation leads to updip extension and pressure-driven salt flow, which are balanced downdip by diapir shortening, salt inflation and advance of the salt nappe (Figures 3–5 and 7). Updip extension, characterized by development of large

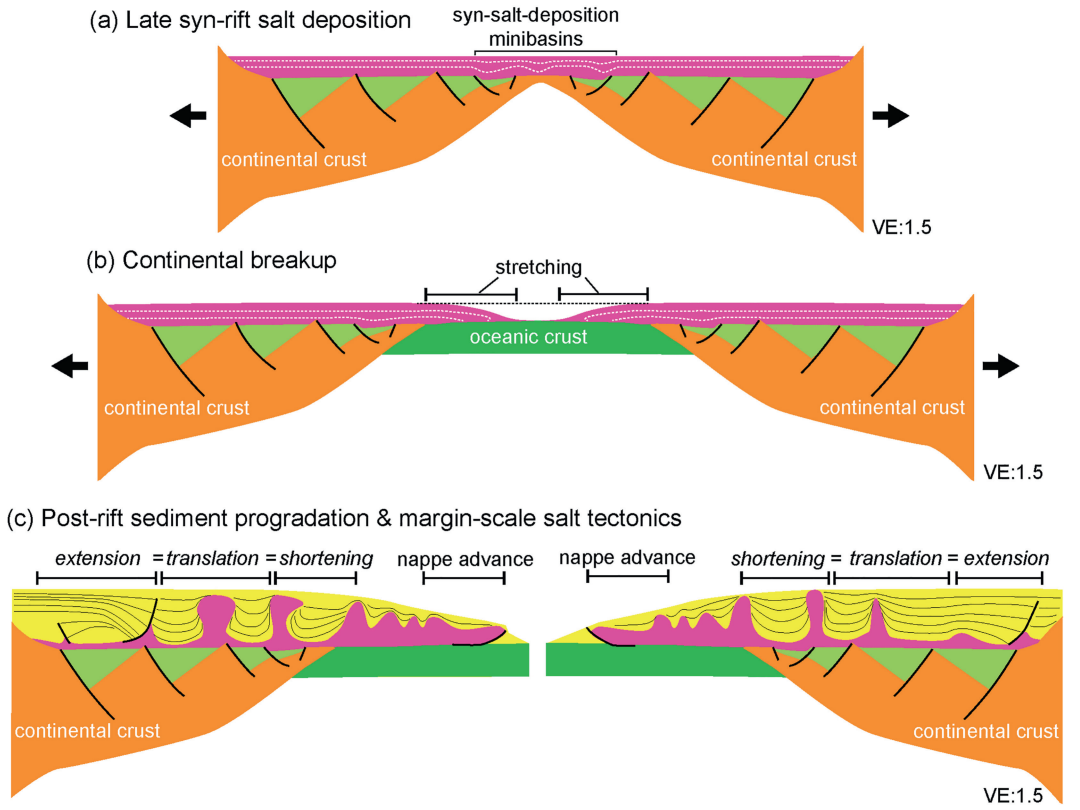

Figure 7. Conceptual diagram illustrating the birth and evolution of rifted margin late syn-rift salt basins. (a) Salt deposition coeval to late-stage extension and continental breakup with syn-salt-deposition minibasins. (b) Distal salt stretching during continental breakup and early ocean spreading, resulting in 10–20 km of wide allochthonous salt nappe on oceanic crust. (c) Post-rift sediment progradation leading to salt tectonics characterized by updip extension, diapirism and minibasin formation in the intermediate margin domain, downdip diapir shortening, salt inflation and advance of the salt nappe.

listric normal faults and rollovers overlying highly depleted salt, is controlled by shear-driven (Couette) salt flow combined with failure and translation of the post-rift overburden. Extension is balanced by salt and overburden translation and downdip shortening, which produces squeezed diapirs, salt tongues and rotated minibasins in the distal domain (Figures 3–5). Balancing of salt deformation in our models shows that post-rift distal nappe advance and salt inflation are largely controlled by lateral pressure-driven (Poiseuille) flow of the salt, which becomes increasingly important with decreasing salt viscosity (Figures 3–6). This explains why the low-viscosity salt model does not show an increase in updip extension and diapir squeezing relative to the reference model as the low-viscosity salt is readily expelled seaward with little overburden extension and translation (Figure 4). The quantitative insight on the balance of salt deformation for rifted margins derived from these models can be used when interpreting natural systems to constrain the various contributions of salt tectonic processes.

The occurrence of these distinct deformation processes (e.g., updip extension, translation, downdip shortening, syn-rift nappe stretching and post-rift nappe advance) is independent of salt viscosity, however their magnitude, timing as well as the style of salt deformation vary (Figures 3–5, Supplementary videos). Other parameters such as (a) the width and architecture of the rifted margin, (b) the timing of salt deposition, (c) variations in syn-rift sediment and salt thickness, and (d) post-salt sedimentation rates may also have an impact and are thus worthy being investigated in future work.

4.2. Comparison With Natural Systems

Our model results are comparable to various natural systems, in particular to the wide salt-bearing margins of the South and Central Atlantic and the Gulf of Mexico, which are the largest and most economically important salt basins known-to-date (Figures 1a–1c) (Lentini et al., 2010; Davison et al., 2012; Hudec et al., 2013; Rowan, 2014, 2020; Kukla et al., 2018). The bulk of salt deformation along these margins occurs in the first ~10–60 Myr of the

post-rift and is associated with deposition of, on average, a ~6–8 km thick prograding succession (Figures 1a–1c) (Davison et al., 2012; Hudec & Jackson, 2004; Peel, 2014; Pichel & Jackson, 2020).

The distribution of salt-tectonic domains of updip extension, translation, downdip diapir shortening, and nappe advance, as well as the magnitudes and style of rifting and salt tectonic deformation observed in our models are similar to what is recognized along these margins (Figures 1a–1c). The updip extensional domain is characterized by minor salt diapirism and the development of listric normal faults associated with salt rollers and rollovers in both models and nature (Figures 1a–1c). Post-salt updip extension and translation range between 13 and 32 km over ~40–60 Myr of post-rift evolution in the salt basins of Brazil and West Africa (Figures 1a–1c) (Erdi & Jackson, 2021; do Amarante et al., 2021; Hudec & Jackson, 2004; Pichel et al., 2018). Estimated values of salt-related updip extension in the range 40–70 km in the Gulf of Mexico are less well constrained owing to its longer history (>100 Myr) and more complex salt tectonics (Hudec & Norton, 2019; Hudec et al., 2013). The magnitude of updip extension in the models is smaller than observed along these margins as we do not simulate their entire >100 Myr post rift evolution, and do not include additional factors such as post-rift continental uplift (e.g., Kwanza Basin, Hudec & Jackson, 2004) or magmatism (Magee et al., 2021). The intermediate translational domain is characterized by early salt inflation, overburden translation, and multiphase diapirism as observed in most, if not all, Brazilian and West Africa rifted margin salt basins (Figures 1a–1c). The magnitudes of overburden extension and translation inferred for these margins are to first-order consistent with the magnitudes of updip extension in our models, for example, 13–32 km for the South Atlantic margins (Dooley et al., 2017; Hudec & Jackson, 2004; Pichel et al., 2018, 2019) .

The distal domain in our models is characterized mainly by squeezed, complex-shaped diapirs associated with seaward-verging salt tongues and rotated minibasins with highly upturned and/or overturned near-diapir strata and, secondarily, by buckle-folding over the distal nappe (Figures 3–5). This is comparable to most of the West Africa salt-bearing margin, including the Kwanza-Lower Congo and Gabon margins, and the Gulf of Mexico (Epin et al., 2021; Hudec & Norton, 2019; Hudec et al., 2013; Lentini et al., 2010; Pilcher et al., 2011; Rowan, 2014). The Brazilian salt basins, in particular the Santos Basin, do not have as much diapir and minibasin complexity in the distal domain owing to highly heterogeneous and stronger salt sequences and are thus more comparable to the high-viscosity salt model (Figures 1b, c, and 6) (Davison et al., 2012; Jackson, Jackson, Hudec, et al., 2015; Pichel et al., 2018; Rodriguez et al., 2018). Estimates of the magnitude of shortening are much harder to obtain for natural systems owing to the common cryptic shortening of diapirs (cf. Rowan & Ratliff, 2012; Figure 1c in Jackson, Jackson, & Hudec, 2015; Jackson, Jackson, Hudec, & Rodriguez, 2015) and are often based on the magnitudes of updip extension for these linked systems, with values ranging between 10 and 20 km (Hudec et al., 2013; Quirk et al., 2012).

The distal edge of the salt in our models is characterized by an allochthonous salt nappe, that overlies newly formed oceanic crust, and varies in complexity and width (15–56 km) depending on salt viscosity (Figures 3–6). The range of nappe widths fits with what is observed in natural examples of wide margins in the West African Kwanza-Lower Congo Basins (20–28 km), the Brazilian Espirito-Santo, Campos and Santos Basins (10–36 km), and the Gulf of Mexico (15–60 km) (Davison et al., 2012; Hudec & Norton, 2019; Hudec et al., 2013; Kukla et al., 2018; Rowan, 2020). Stratigraphic onlap of post-salt sediments onto the seaward end of the nappes indicate that they form relatively early during salt tectonic evolution (cf. Davison et al., 2012; Epin et al., 2021; Rowan, 2014), which implies that their advance is at least partially unrelated to the longer-lived post-rift updip extension. This agrees with our models and suggests that the salt nappes along these margins are also formed by a combination of late syn-rift stretching and post-rift advance by Poiseuille flow.

Features described at the continent-ocean transition in parts of West Africa, Brazil, and Gulf of Mexico such as volcanic edifices (Fernandez et al., 2020), exhumed mantle (Rowan, 2014; Zalán et al., 2011) or the so-called oceanic crust step-ups (Rowan, 2020) do not form in our models. Although these could have an impact on the final width of the nappe, the processes operating in its evolution, that is, syn-rift stretching and post-rift advance, are likely be the same as long the salt is continuous over the distal margin. Temperature-dependent salt viscosity is also not included in our models for simplification purposes. This would promote a localized decrease in salt viscosity over the rift axis where the geotherms are shallower, which would likely enhance syn-rift stretching and thus produce wider salt nappes as in the low-viscosity salt model (Figure 4).

Variations in salt viscosity provide a first-order control on the style and magnitude of salt tectonics and on the dimensions of distal salt nappes and may explain some of the differences observed in natural systems. However, additional factors not included here such as varying rifted margin geometry, salt and pre-salt sediment thickness, post-salt sedimentation, intra-salt rheological variability, as well as 3D salt flow, temperature-dependent salt viscosity and syn-rift magmatism are also likely to play a role in modulating salt tectonics on rifted margins and are thus worthy to be investigated in the future.

5. Conclusions

Our models improve current understanding of the dynamics of salt tectonics along rifted margins and the interplay between rifting and syn- to post-rift salt deformation associated with late syn-rift salt basins. In their proximal domains, where salt is deposited above inactive rift structures, they remain largely undeformed until post-rift times. The distal salt undergoes stretching associated with continental breakup and early oceanic spreading during and soon after its deposition. This produces widening of the salt basin, syn-salt-deposition intra-salt minibasins and development of an allochthonous salt nappe over newly formed oceanic crust. The margin is subsequently affected by pronounced salt tectonics characterized by updip extension, translation, downdip shortening, and pressure-driven salt nappe advance, all resulting from the seaward tilt of the margin and post-rift sediment progradation. The nappe that was initiated by syn-rift stretching advances further by pressure-driven Poiseuille salt flow so that the final width of the nappe is a product of late syn-rift salt stretching and post-rift pressure-driven salt flow. The models show that updip extension balances largely with downdip diapir shortening indicating that the post-rift salt nappe advance is mostly controlled by pressure-driven Poiseuille salt flow. This implies that the present-day width of salt nappes cannot be used as a constraint to balance updip extension on salt-bearing rifted margins. These observations have important implications for kinematic reconstructions of salt tectonics along these margins based on the common assumption of balanced salt deformation and for understanding the relationship between the distal edge of the salt basin and continent-ocean boundaries, important for plate-kinematic reconstructions. The models are comparable to various examples of wide salt-bearing rifted margins such as the Brazilian, parts of West Africa, and Gulf of Mexico salt basins. They reproduce their observed crustal-scale architecture, regional salt tectonics styles, distribution of structural domains, magnitudes of deformation, and elucidate the dynamics of regional salt deformation and the interplay between rifting, margin architecture, salt deposition and tectonics.

Data Availability Statement

Data are computed with the equations presented here and in the Supporting Information S1. All model outputs, graphics and time-steps are presented as animations in the Supporting Information S1 and in the Dataverse repository: https://dataverse.no/dataset.xhtml?persistentId=doi:10.18710/A2YX9V.

Acknowledgments
We thank the Equinor-UiB Akademia agreement for funding. We thank Uninett Sigma2 for computing time of project NN4704K. We thank Christopher Jackson, Mike Hudec and Oscar Fernandes for the very detailed and constructive reviews, which helped significantly to improve this paper. We also thank Oriol Ferrer for the insightful discussions during the preparation of this manuscript.

References

Albertz, M., & Ings, S. J. (2012). Some consequences of mechanical stratification in basin-scale numerical models of passive-margin salt tectonics. *Geological Society, London, Special Publications*, *363*(1), 303–330.

Allen, J., & Beaumont, C. (2016). Continental margin syn-rift salt tectonics at intermediate width margins. *Basin Research*, *28*(5), 598–633. https://doi.org/10.1111/bre.12123

Allen, J., Beaumont, C., & Deptuck, M. E. (2020). Feedback between syn-rift lithospheric extension, sedimentation and salt tectonics on wide, weak continental margins. *Petroleum Geoscience*, *26*(1), 16–35. https://doi.org/10.1144/petgeo2018-089

Baby, G., Guillocheau, F., Braun, J., Robin, C., & Dall'Asta, M. (2020). Solid sedimentation rates history of the Southern African continental margins: Implications for the uplift history of the South African Plateau. *Terra Nova*, *32*(1), 53–65. https://doi.org/10.1111/ter.12435

Blaich, O. A., Faleide, J. I., & Tsikalas, F. (2011). Crustal breakup and continent-ocean transition at South Atlantic conjugate margins. *Journal of Geophysical Research*, *116*(B1), B01402. https://doi.org/10.1029/2010jb007686

Brun, J. P., & Fort, X. (2011). Salt tectonics at passive margins: Geology versus models. *Marine and Petroleum Geology*, *28*(6), 1123–1145. https://doi.org/10.1016/j.marpetgeo.2011.03.004

Buck, W. R. (1993). Effect of lithospheric thickness on the formation of high-and low-angle normal faults. *Geology*, *21*(10), 933–936. https://doi.org/10.1130/0091-7613(1993)021<0933:eoltot>2.3.co;2

Burrel, L., & Teixell, A. (2021). Contractional salt tectonics and role of pre-existing diapiric structures in the Southern Pyrenean foreland fold–thrust belt (Montsec and Serres Marginals). *Journal of the Geological Society*, *178*(4), jgs2020. https://doi.org/10.1144/jgs2020-085

Curry, M. A., Peel, F. J., Hudec, M. R., & Norton, I. O. (2018). Extensional models for the development of passive-margin salt basins, with application to the Gulf of Mexico. *Basin Research*, *30*(6), 1180–1199. https://doi.org/10.1111/bre.12299

Davison, I., Anderson, L., & Nuttall, P. (2012). Salt deposition, loading and gravity drainage in the Campos and Santos salt basins. *Geological Society of London Special Publications*, *363*(1), 159–174. https://doi.org/10.1144/sp363.8

do Amarante, F. B., Jackson, C. A. L., Pichel, L. M., Scherer, C. M. D. S., & Kuchle, J. (2021). Pre-salt rift morphology controls salt tectonics in the Campos Basin, offshore SE Brazil. *Basin Research*, *33*(5), 2837–2861. https://doi.org/10.1111/bre.12588

Dooley, T. P., Hudec, M. R., Carruthers, D., Jackson, M. P., & Luo, G. (2017). The effects of base-salt relief on salt flow and suprasalt deformation patterns—Part 1: Flow across simple steps in the base of salt. *Interpretation*, *5*(1), SD1–SD23. https://doi.org/10.1190/int-2016-0087.1

Dooley, T. P., Hudec, M. R., Pichel, L. M., & Jackson, M. P. (2018). The impact of base-salt relief on salt flow and suprasalt deformation patterns at the autochthonous, paraautochthonous and allochthonous level: Insights from physical models. *Geological Society, London, Special Publications*, *476*(1), 287. https://doi.org/10.1144/sp476.13

Epin, M. E., Manatschal, G., Sapin, F., & Rowan, M. G. (2021). The tectono-magmatic and subsidence evolution during lithospheric breakup in a salt-rich rifted margin: Insights from a 3D seismic survey from southern Gabon. *Marine and Petroleum Geology*, *128*, 105005. https://doi.org/10.1016/j.marpetgeo.2021.105005

Erdi, A., & Jackson, C. A. L. (2021). What controls salt-detached contraction in the translational domain of the outer Kwanza Basin, offshore Angola? *Basin Research*, *33*(3), 1880–1905. https://doi.org/10.1111/bre.12539

Erdős, Z., Huismans, R. S., van der Beek, P., & Thieulot, C. (2014). Extensional inheritance and surface processes as controlling factors of mountain belt structure. *Journal of Geophysical Research: Solid Earth*, *119*(12), 9042–9061. https://doi.org/10.1002/2014jb011408

Evain, M., Afilhado, A., Rigoti, C., Loureiro, A., Alves, D., Klingelhoefer, F., et al. (2015). Deep structure of the Santos basin-São Paulo plateau system, SE Brazil. *Journal of Geophysical Research: Solid Earth*, *120*(8), 5401–5431. https://doi.org/10.1002/2014jb011561

Fernandez, N., Hudec, M. R., Jackson, C. A. L., Dooley, T. P., & Duffy, O. B. (2020). The competition for salt and kinematic interactions between minibasins during density-driven subsidence: Observations from numerical models. *Petroleum Geoscience*, *26*(1), 3–15. https://doi.org/10.1144/petgeo2019-051

Ford, M., & Vergés, J. (2021). Evolution of a salt-rich transtensional rifted margin, eastern North Pyrenees, France. *Journal of the Geological Society*, *178*(1), jgs2019–157. https://doi.org/10.1144/jgs2019-157

Gemmer, L., Ings, S. J., Medvedev, S., & Beaumont, C. (2004). Salt tectonics driven by differential sediment loading: Stability analysis and finite-element experiments. *Basin Research*, *16*(2), 199–218. https://doi.org/10.1111/j.1365-2117.2004.00229.x

Gleason, G. C., & Tullis, J. (1995). A flow law for dislocation creep of quartz aggregates determined with the molten salt cell. *Tectonophysics*, *247*(1–4), 1–23. https://doi.org/10.1016/0040-1951(95)00011-b

Goteti, R., Beaumont, C., & Ings, S. J. (2013). Factors controlling early stage salt tectonics at rifted continental margins and their thermal consequences. *Journal of Geophysical Research: Solid Earth*, *118*(6), 3190–3220. https://doi.org/10.1002/jgrb.50201

Hossack, J. (1995). Geometric rules of section balancing for salt structures. In M. P. A. Jackson, D. G. Roberts, & S. Snelson (Eds.) *Salt Tectonics: a Global Perspective American Association of Petroleum Geologists Memoir* (Vol. 65, pp. 29–40).

Hudec, M. R., & Jackson, M. P. (2004). Regional restoration across the Kwanza Basin, Angola: Salt tectonics triggered by repeated uplift of a metastable passive margin. *AAPG Bulletin*, *88*(7), 971–990. https://doi.org/10.1306/02050403061

Hudec, M. R., & Norton, I. O. (2019). Upper Jurassic structure and evolution of the Yucatán and Campeche subbasins, southern Gulf of Mexico. *AAPG Bulletin*, *103*(5), 1133–1151. https://doi.org/10.1306/11151817405

Hudec, M. R., Norton, I. O., Jackson, M. P., & Peel, F. J. (2013). Jurassic evolution of the Gulf of Mexico salt basin. *AAPG Bulletin*, *97*(10), 1683–1710. https://doi.org/10.1306/04011312073

Huismans, R. S., & Beaumont, C. (2002). Asymmetric lithospheric extension: The role of frictional plastic strain softening inferred from numerical experiments. *Geology*, *30*(3), 211–214. https://doi.org/10.1130/0091-7613(2002)030<0211:aletro>2.0.co;2

Huismans, R. S., & Beaumont, C. (2011). Depth-dependent extension, two-stage breakup and cratonic underplating at rifted margins. *Nature*, *473*(7345), 74–78. https://doi.org/10.1038/nature09988

Huismans, R. S., & Beaumont, C. (2014). Rifted continental margins: The case for depth-dependent extension. *Earth and Planetary Science Letters*, *407*, 148–162. https://doi.org/10.1016/j.epsl.2014.09.032

Jackson, C. A. L., Jackson, M. P., & Hudec, M. R. (2015). Understanding the kinematics of salt-bearing passive margins: A critical test of competing hypotheses for the origin of the Albian Gap, Santos Basin, offshore Brazil. *Bulletin*, *127*(11–12), 1730–1751. https://doi.org/10.1130/b31290.1

Jackson, C. A. L., Jackson, M. P., Hudec, M. R., & Rodriguez, C. R. (2015). Enigmatic structures within salt walls of the Santos Basin—Part 1: Geometry and kinematics from 3D seismic reflection and well data. *Journal of Structural Geology*, *75*, 135–162. https://doi.org/10.1016/j.jsg.2015.01.010

Jackson, M. P., & Hudec, M. R. (2017). *Salt tectonics: Principles and practice*. Cambridge University Press.

Karato, S.-I., & Wu, P. (1993). Rheology of the upper mantle: A synthesis. *Science*, *260*(5109), 771–778. https://doi.org/10.1126/science.260.5109.771

Kukla, P. A., Strozyk, F., & Mohriak, W. U. (2018). South Atlantic salt basins–witnesses of complex passive margin evolution. *Gondwana Research*, *53*, 41–57. https://doi.org/10.1016/j.gr.2017.03.012

Kumar, N., Danforth, A., Nuttall, P., Helwig, J., Bird, D. E., & Venkatraman, S. (2013). From oceanic crust to exhumed mantle: A 40 year (1970–2010) perspective on the nature of crust under the Santos Basin, SE Brazil. *Geological Society, London, Special Publications*, *369*(1), 147–165. https://doi.org/10.1144/sp369.16

Lavier, L. L., Buck, W. R., & Poliakov, A. N. (2000). Factors controlling normal fault offset in an ideal brittle layer. *Journal of Geophysical Research*, *105*(B10), 23431–23442. https://doi.org/10.1029/2000jb900108

Lavier, L. L., Roger Buck, W., & Poliakov, A. N. (1999). Self-consistent rolling-hinge model for the evolution of large-offset low-angle normal faults. *Geology*, *27*(12), 1127–1130. https://doi.org/10.1130/0091-7613(1999)027<1127:scrhmf>2.3.co;2

Lentini, M. R., Fraser, S. I., Sumner, H. S., & Davies, R. J. (2010). Geodynamics of the central South Atlantic conjugate margins: Implications for hydrocarbon potential. *Petroleum Geoscience*, *16*(3), 217–229. https://doi.org/10.1144/1354-079309-909

Lu, G., & Huismans, R. S. (2022). Magmatism at passive margins: Effects of depth-dependent wide rifting and lithospheric counterflow. *Journal of Geophysical Research: Solid Earth*, *127*(3), e2021JB023046. https://doi.org/10.1029/2021jb023046

Magee, C., Pichel, L. M., Madden-Nadeau, A. L., Jackson, C. A. L., & Mohriak, W. (2021). Salt–magma interactions influence intrusion distribution and salt tectonics in the Santos Basin, offshore Brazil. *Basin Research*, *33*(3), 1820–1843. https://doi.org/10.1111/bre.12537

Marton, L. G., Tari, G. C., & Lehmann, C. T. (2000). Evolution of the Angolan passive margin, West Africa, with emphasis on post-salt structural styles. *Geophysical Monograph-American Geophysical Union*, *115*, 129–150.

Norton, I. O., Carruthers, D. T., & Hudec, M. R. (2016). Rift to drift transition in the South Atlantic salt basins: A new flavor of oceanic crust. *Geology*, *44*(1), 55–58. https://doi.org/10.1130/g37265.1

Peel, F. J. (2014). The engines of gravity-driven movement on passive margins: Quantifying the relative contribution of spreading vs. gravity sliding mechanisms. *Tectonophysics*, *633*, 126–142. https://doi.org/10.1016/j.tecto.2014.06.023

Peel, F. J., Travis, C. J., & Hossack, J. R. (1995). Genetic structural provinces and salt tectonics of the Cenozoic offshore US Gulf of Mexico: A preliminary analysis. In M. P. A. Martin, D. G. Roberts, & S. Snelson (Eds.) *Salt Tectonics: A Global Perspective* (Vol. 65, pp. 153–175). AAPG Memoir.

Pichel, L. M., Finch, E., & Gawthorpe, R. L. (2019). The impact of pre-salt rift topography on salt tectonics: A discrete-element modeling approach. *Tectonics*, *38*(4), 1466–1488. https://doi.org/10.1029/2018tc005174

Pichel, L. M., & Jackson, C. A. L. (2020). The enigma of the Albian Gap: Spatial variability and the competition between salt expulsion and extension. *Journal of the Geological Society*, *177*(6), 1129–1148. https://doi.org/10.1144/jgs2020-055

Pichel, L. M., Jackson, C. A. L., Peel, F., & Dooley, T. P. (2020). Base-salt relief controls salt-tectonic structural style, São Paulo Plateau, Santos Basin, Brazil. *Basin Research*, *32*(3), 453–484. https://doi.org/10.1111/bre.12375

Pichel, L. M., Jackson, C. A. L., Peel, F., & Ferrer, O. (2021). The Merluza Graben: How a failed spreading center influenced margin structure, and salt deposition and tectonics in the Santos Basin, Brazil. *Tectonics*, *40*(10), e2020TC006640. https://doi.org/10.1029/2020tc006640

Pichel, L. M., Peel, F., Jackson, C. A.-L., & Huuse, M. (2018). Geometry and kinematics of salt-detached ramp syncline basins. *Journal of Structural Geology*, *115*, 208–230. https://doi.org/10.1016/j.jsg.2018.07.016

Pilcher, R. S., Kilsdonk, B., & Trude, J. (2011). Primary basins and their boundaries in the deep-water northern Gulf of Mexico: Origin, trap types, and petroleum system implications. *AAPG Bulletin*, *95*(2), 219–240. https://doi.org/10.1306/06301010004

Pysklywec, R. N., & Beaumont, C. (2004). Intraplate tectonics: Feedback between radioactive thermal weakening and crustal deformation driven by mantle lithosphere instabilities. *Earth and Planetary Science Letters*, *221*(1–4), 275–292. https://doi.org/10.1016/s0012-821x(04)00098-6

Quirk, D. G., Schødt, N., Lassen, B., Ings, S. J., Hsu, D., Hirsch, K. K., & Von Nicolai, C. (2012). Salt tectonics on passive margins: Examples from Santos, Campos and Kwanza basins. *Geological Society, London, Special Publications*, *363*(1), 207–244. https://doi.org/10.1144/SP363.10

Roca, E., Ferrer, O., Rowan, M. G., Muñoz, J. A., Butillé, M., Giles, K. A., et al. (2021). Salt tectonics and controls on halokinetic-sequence development of an exposed deepwater diapir: The Bakio Diapir, Basque-Cantabrian Basin, Pyrenees. *Marine and Petroleum Geology*, *123*, 104770. https://doi.org/10.1016/j.marpetgeo.2020.104770

Rodriguez, C. R., Jackson, C. L., Rotevatn, A., Bell, R. E., & Francis, M. (2018). Dual tectonic-climatic controls on salt giant deposition in the Santos Basin, offshore Brazil. Geosphere. *Geosphere*, *14*(1), 215–242. https://doi.org/10.1130/ges01434.1

Rowan, M. G. (2014). Passive-margin salt basins: Hyperextension, evaporite deposition, and salt tectonics. *Basin Research*, *26*(1), 154–182. https://doi.org/10.1111/bre.12043

Rowan, M. G. (2020). The South Atlantic and Gulf of Mexico salt basins: Crustal thinning, subsidence and accommodation for salt and presalt strata. *Geological Society, London, Special Publications*, *476*(1), 333–363. https://doi.org/10.1144/sp476.6

Rowan, M. G., Peel, F. J., & Vendeville, B. C. (2004). Gravity-driven fold-belts on passive margins.

Rowan, M. G., & Ratliff, R. A. (2012). Cross-section restoration of salt-related deformation: Best practices and potential pitfalls. *Journal of Structural Geology*, *41*, 24–37. https://doi.org/10.1016/j.jsg.2011.12.012

Tari, G., Novotny, B., Jabour, H., & Hafid, M. (2017). Salt tectonics along the Atlantic margin of NW Africa (Morocco and Mauritania). In *Permo-Triassic Salt Provinces of Europe, North Africa and the Atlantic Margins* (pp. 331–351). Elsevier.

Theunissen, T., & Huismans, R. S. (2019). Long-term coupling and feedback between tectonics and surface processes during non-volcanic rifted margin formation. *Journal of Geophysical Research: Solid Earth*, *124*(11), 12323–12347. https://doi.org/10.1029/2018jb017235

Thieulot, C. (2011). FANTOM: Two-and three-dimensional numerical modeling of creeping flows for the solution of geological problems. *Physics of the Earth and Planetary Interiors*, *188*(1–2), 47–68. https://doi.org/10.1016/j.pepi.2011.06.011

Turcotte, D. L., & Schubert, G. (2002). *Geodynamics*. Cambridge University Press.

Unternehr, P., Péron-Pinvidic, G., Manatschal, G., & Sutra, E. (2010). Hyper-extended crust in the South Atlantic: In search of a model. *Petroleum Geoscience*, *16*(3), 207–215. https://doi.org/10.1144/1354-079309-904

Urai, J. L., Schléder, Z., Spiers, C. J., & Kukla, P. A. (2008). Flow and transport properties of salt rocks. In *Dynamics of complex intracontinental basins: The central European basin system* (pp. 277–290).

van Keken, P. E., Spiers, C. J., Van den Berg, A. P., & Muyzert, E. J. (1993). The effective viscosity of rocksalt: Implementation of steady-state creep laws in numerical models of salt diapirism. *Tectonophysics*, *225*(4), 457–476. https://doi.org/10.1016/0040-1951(93)90310-g

Walker, O. A., Alves, T. M., Hesselbo, S. P., Pharaoh, T., Nuzzo, M., & Mattos, N. H. (2021). Significance of Upper Triassic to Lower Jurassic salt in the identification of palaeo-seaways in the North Atlantic. *Marine and Petroleum Geology*, *123*, 104705. https://doi.org/10.1016/j.marpetgeo.2020.104705

Zalán, P. V., Severino, M. D. C. G., Rigoti, C. A., Magnavita, L. P., De Oliveira, J. A. B., & Vianna, A. R. (2011). An entirely new 3D-view of the crustal and mantle structure of a South Atlantic passive margin—Santos, Campos and Espírito Santo basins, Brazil. In *AAPG Annual Convention and Exhibition, Houston, Texas*.

References From the Supporting Information

Willett, S. D. (1992). Dynamic and kinematic growth and change of a Coulomb wedge. In K. R. McClay (Ed.), *Thrust tectonics* (pp. 19–31). Springer Netherlands. https://doi.org/10.1007/978-94-011-3066-0